Isospin Pomeranchuk effect in twisted bilayer graphene

https://doi.org/10.1038/s41586-021-03409-2

Received: 25 August 2020

Accepted: 26 February 2021

Published online: 7 April 2021



Check for updates

Yu Saito^{1,2,7}, Fangyuan Yang^{1,7}, Jingyuan Ge¹, Xiaoxue Liu³, Takashi Taniguchi⁴, Kenji Watanabe⁵, J. I. A. Li³, Erez Berg⁶ & Andrea F. Young^{1⊠}

In condensed-matter systems, higher temperatures typically disfayour ordered phases, leading to an upper critical temperature for magnetism, superconductivity and other phenomena. An exception is the Pomeranchuk effect in ³He, in which the liquid ground state freezes upon increasing the temperature¹, owing to the large entropy of the paramagnetic solid phase. Here we show that a similar mechanism describes the finite-temperature dynamics of spin and valley isospins in magic-angle twisted bilayer graphene². Notably, a resistivity peak appears at high temperatures near a superlattice filling factor of -1, despite no signs of a commensurate correlated phase appearing in the low-temperature limit. Tilted-field magnetotransport and thermodynamic measurements of the in-plane magnetic moment show that the resistivity peak is connected to a finite-field magnetic phase transition³ at which the system develops finite isospin polarization. These data are suggestive of a Pomeranchuk-type mechanism, in which the entropy of disordered isospin moments in the ferromagnetic phase stabilizes the phase relative to an isospin-unpolarized Fermi liquid phase at higher temperatures. We find the entropy, in units of Boltzmann's constant, to be of the order of unity per unit cell area, with a measurable fraction that is suppressed by an in-plane magnetic field consistent with a contribution from disordered spins. In contrast to ³He, however, no discontinuities are observed in the thermodynamic quantities across this transition. Our findings imply a small isospin stiffness^{4,5}, with implications for the nature of finite-temperature electron transport⁶⁻⁸, as well as for the mechanisms underlying isospin ordering and superconductivity^{9,10} in twisted bilayer graphene and related systems.

The best-studied example of moiré flat-band systems², magic-angle twisted bilayer graphene¹¹, is known to host a wide array of low-temperature phases^{3,9,10,12-16}. Some among these, notably correlated insulators^{3,10,12} and orbital Chern ferromagnets^{3,13,17,18}, are known to unambiguously arise from the effects of the Coulomb interaction. However, the origin of other phenomena is less clear, particularly superconductivity^{3,9,10,14-16} and the large scattering observed in the metallic finite-temperature state^{6,7}. The prevalence of Coulomb-driven phases suggests a unified origin for all of the phenomenology. In this picture both superconductivity and the finite-temperature resistivity would arise from the interaction of charge carriers with collective modes of the spin and valley isospin. However, theoretical efforts based on conventional phononic mechanisms do appear to capture the basic experimental phenomenology of both the superconducting¹⁹⁻²² and high-temperature metallic states²³. We report here an entropically driven phase transition between an isospin-unpolarized Fermi liquid at low temperature and a state characterized by large, strongly fluctuating local magnetic moments at high temperature. Although no such phenomenology is expected from electron-phonon interactions alone, our results imply the existence of low-energy collective modes of electronic origin that couple strongly to the charge carriers. Such modes probably have a crucial role in determining the low-temperature phase diagram as well as the finite-temperature transport properties.

Low- and intermediate-temperature transport

Figure 1 shows transport measurements performed on a highly homogeneous twisted bilayer graphene device fabricated with inter-layer twist angle $\theta \approx 1.12^{\circ}$ (ref. ²⁴; see Extended Data Fig. 1). Figure 1a shows the magnetoresistance measured at 0.4 K, plotted as a function of the nominal electron filling v_0 of the superlattice unit cell and an applied out-of-plane magnetic field B_{\perp} . We determine v_0 from the geometric capacitance, measured from the Hall density near charge neutrality, and the positions of the most prominent resistivity features at $B_{\perp} = 0$ T, which we associate with filling factors v = -2, +2 and +3. For B_{\perp} of 1–2 T, distinct sets of quantum oscillations are observed at low magnetic fields that intersect the $B_1 = 0$ axis at $v_0 = -3$, -2 and 0 and show one fold, twofold, and fourfold degeneracy, respectively (see also Supplementary

Department of Physics, University of California at Santa Barbara, Santa Barbara, CA, USA, 2 California NanoSystems Institute, University of California at Santa Barbara, Santa Barbara, CA, USA, 2 California NanoSystems Institute, University of California at Santa Barbara, Santa Barbara, CA, USA, 2 California NanoSystems Institute, University of California at Santa Barbara, Santa Barbara, CA, USA, 2 California NanoSystems Institute, University of California at Santa Barbara, Santa Barbara, CA, USA, 2 California NanoSystems Institute, University of California at Santa Barbara, Santa Barbara, CA, USA, 3 California NanoSystems Institute, University of California at Santa Barbara, Santa Barbara, CA, USA, 3 California NanoSystems Institute, University of California NanoSystems Institute, Univer 3Department of Physics, Brown University, Providence, RI, USA, 4International Center for Materials Nanoarchitectonics, National Institute for Materials Science, Tsukuba, Japan, 5Research Center for Functional Materials, National Institute for Materials Science, Tsukuba, Japan. Department of Condensed Matter Physics, Weizmann Institute of Science, Rehovot, Israel. These authors contributed equally: Yu Saito, Fangyuan Yang. [™]e-mail: andrea@physics.ucsb.edu

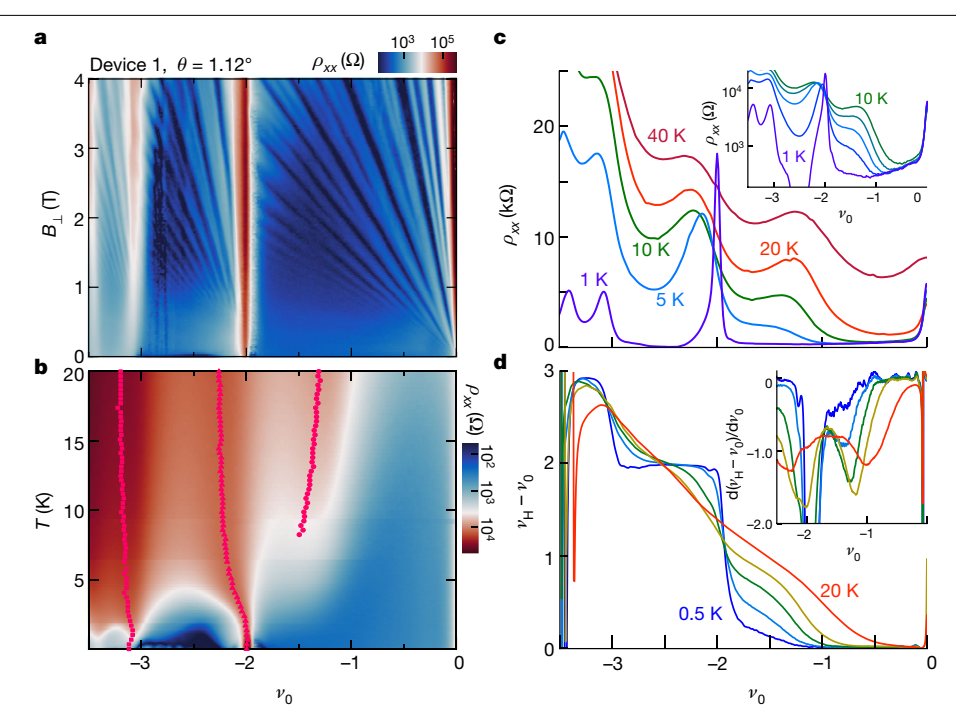


Fig. 1 | Contrasting transport at low and intermediate temperatures in **twisted bilayer graphene near** $v_0 = -1$. **a**, Longitudinal resistivity ρ_{xx} in device 1 as a function of the nominal superlattice filling factor v_0 and out-of-plane magnetic field B_{\perp} , acquired at T = 400 mK. No correlated state is observed at $v_0 = -1$ Additional analysis of low-B data, as well as data from device 2, are shown in Supplementary Figs. 1, 5. **b**, ρ_{xx} as a function of temperature T and v_0 at

 $B_{\text{tot}} = 0$ T in device 1. Pink circles correspond to the position of the local maxima $in \rho_{xx}$. A resistivity peak emerges near $v_0 = -1$ above T = 5 K. \mathbf{c}, ρ_{xx} traces at T = 1, 5, 10, 20 and 40 K and $B_{\text{tot}} = 0$ T. Inset, ρ_{xx} traces at T = 1, 3, 5, 7 and 10 K and $B_{\text{tot}} = 0$ T, plotted on a logarithmic scale. **d**, Hall density $v_H - v_0$ as a function of v_0 at T =0.5, 2.5, 4.5, 8.0 and 20.0 K and B_{\perp} = 0.5 T. Inset, $d(\nu_H - \nu_0)/d\nu_0$ as a function of ν_0 .

Fig. 1). In graphene systems, spin and valley degeneracy typically give rise to quantum oscillations with degeneracy of four. The lower degeneracy of the quantum oscillations originating from $v_0 = -2$ and -3 are consistent with ferromagnetism in which the ground states near those filling are polarized into one isospin flavour for $-4 < v_0 < -3$ or two flavours for $-3 < v_0 < -2$ (ref. ²⁵). No comparable 'fan' is observed at low B_{\perp} with intercept at $v_0 = -1$, and the quantum oscillations originating from the charge neutrality point maintain apparent fourfold degeneracy for $-2 < v_0 < 0$, suggesting unbroken flavour symmetry in that regime.

The primary unexplained experimental phenomenology is illustrated in Fig. 1b, c, which shows transport data from the same device at higher temperatures. Near $v_0 = -3$ and $v_0 = -2$, resistivity peaks associated with low-temperature correlated phases weaken and depin from commensurate v as the temperature is raised. In addition, they are joined by a third resistivity peak near—but not at— v_0 = -1. By 40 K, these peaks are indistinguishable, pointing to a universal behaviour at this temperature. We observe very similar behaviour in a second device with $\theta = 1.06^{\circ}$ (device 2; see Extended Data Figs. 2, 3 and Supplementary Figs. 2, 5). Moreover, this behaviour appears in the published experimental literature on twisted bilayer graphene, where its origin has remained unexplained^{6,16}. Measurements of the Hall density show related behaviour. Figure 1d shows the Hall density v_{H} plotted in units of electrons per unit cell and with the density arising after subtracting the nominal filling factor (v_0). The subtracted Hall density, $v_{\rm H} - v_{\rm o}$, develops a pronounced kink between $v_{\rm o} = -1$ and -2 at high temperature, similar to that seen near $v_0 = -3$ and -2 (see also Extended Data Fig. 3). This is seen clearly in plots of $\frac{d}{dv_0}(v_H - v_0)$ (Fig. 1d, inset), where the kinks appear as extrema. Similar kinks have been associated with symmetry breaking at low temperatures²⁶, specifically a reduction in the isospin symmetry of the Fermi surface. The behaviour of the Hall density and longitudinal resistivity suggest the existence of an isospin-polarized phase at high temperatures that is absent in the zero-temperature limit.

In-plane field-induced magnetization

The connection between high-temperature resistivity peaks and isospin-symmetry breaking is illustrated by the transport behaviour at 20 mK in a magnetic field B_{\parallel} applied in the plane of the sample, which shows remarkably similar behaviour to that at elevated temperature. As shown in Fig. 2a, b, for $B_{\parallel} \gtrsim 3$ T, an additional resistance peak develops for $-2 < v_0 \le -1$, whereas the resistance peak initially at $v_0 = -2$ depins from this filling and decreases in magnitude as it moves to larger absolute v_0 . The Hall density similarly shows the development of a new step near $v_0 = -1$ that is absent at B = 0 T (Extended Data Fig. 4). The behaviour of the resistivity peak is roughly independent of the orientation of the magnetic field, showing nearly identical trajectories for in-plane or partially out-of-plane magnetic fields (Supplementary Fig. 3). Tilted-field data (Supplementary Fig. 4 and Extended Data Fig. 5) reveal that the resistivity peak separates discrete domains of quantum oscillations: for $v_0 > v_{\rm pk}$ (where $v_{\rm pk}$ denotes the filling at the peak in $-2 < v_0 \le -1$) the oscillation minima remain qualitatively unchanged, extrapolating to v_0 = 0, whereas for $v_0 < v_{pk}$ new quantum oscillations emerge that extrapolate to $v_0 = -1$ at B = 0 T. We interpret the resistivity peak as a B_{\parallel} -driven transition from an isospin-unpolarized (IU) paramagnetic state at low B to a spin- and valley-polarized isospin ferromagnetic (IF₃) state at high B in which electrons are polarized into three of four isospin flavours. This hypothesis is also consistent with the observation of a strong Chern insulator state with Chern number $C = \pm 3$ in this regime in an out-of-plane field^{24,27,28}. The additional resistivity peaks associated with $v_0 = -2$ and $v_0 = -3$ at low T similarly denote boundaries between ferromagnetic phases (IF2 and IF1 phases) with fewer occupied isospin flavours.

Near $v = \pm 1$, most proposed ordered ground states are expected to have finite spin polarization, making the in-plane magnetization per unit cell, M_{\parallel} , a good proxy for isospin polarization. To determine M_{\parallel} we use device 2 (ref. 29) the geometry 30,31 of which enables direct

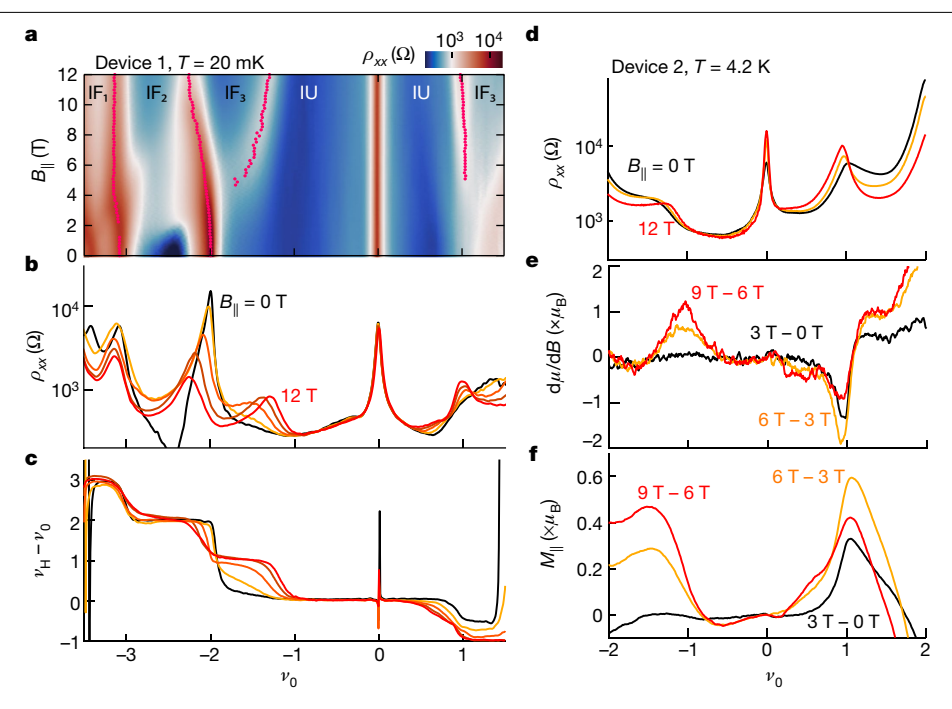


Fig. 2 | **In-plane magnetic-field-stabilized isospin ferromagnetism. a**, ρ_{xx} as a function of v_0 and in-plane magnetic field B_{\parallel} acquired at a nominal temperature of T=20 mK in device 1. Pink circles denote ρ_{xx} peak positions showing phase boundaries between symmetry-breaking isospin ferromagnets (IF₁, IF₂, and IF₃) and an isospin-unpolarized state (IU). **b**, ρ_{xx} as a function of v_0 at $B_{\parallel}=0,3,6,9$ and 12 T. **c**, Subtracted Hall density $v_{\rm H}-v_0$ expressed in electrons per superlattice unit cell, and measured with $B_{\rm tot}=0.5,3,6,9$ and 12 T and fixed

 B_\perp = 0.5 T. **d**, ρ_{xx} as a function of ν_0 at B_\parallel = 0, 6 and 12 T and T = 4.2 K in device 2. **e**, $d\mu/dB$ as a function of ν_0 . Red, orange and black curves are calculated from finite differences of μ in Extended Data Fig. 6a. For brevity, the finite difference between the data at B_\parallel = 9 T and at B_\parallel = 6 T is given by '9 T – 6 T', and so on. **f**, Magnetization per superlattice unit cell as a function of ν_0 , obtained by integrating the data in **e** with respect to ν_0 .

measurement of the chemical potential, μ , of the twisted bilayer graphene layer (see Methods and Extended Data Fig. 1b). M_{\parallel} is then extracted via the Maxwell relation $(\partial M_{\parallel}/\partial v)_{B_{\parallel}} = -(\partial \mu/\partial B_{\parallel})_{\nu}$.

Transport is qualitatively similar between devices 1 and 2; in particular, both devices show a T- or B_{\parallel} -induced resistance peak near $\nu_0 = -1$ that is absent at low temperatures and field (Fig. 2a, Supplementary Fig. 2, Extended Data Fig. 2). In addition, the slightly smaller twist angle in device 2 appears to favour a correlated state at $\nu_0 = +1$ that is absent at B = 0 in device 1 (Extended Data Fig. 2).

 $\partial \mu/\partial B_{\parallel}$ is shown in Fig. 2e, determined using measurements of μ acquired at 3-T intervals. The uncertainty of the repeated scans is shown in Supplementary Fig. 6. The integrated $M_{\parallel} = -\int_{0}^{v_{0}} \frac{\partial \mu}{\partial B_{\parallel}} d\nu$ is shown in Fig. 2f (see also Extended Data Fig. 6). Finite M_{\parallel} is observed at $v_{0} \approx 1$ even at the lowest magnetic fields in device 2, consistent with the resistivity peak seen at the same filling being associated with an isospin ferromagnet with finite spin polarization. This build-up of magnetization near $v_0 = 1$ is consistent with prior observations ^{25,32}. By contrast, near $v_0 = -1$ no magnetization is observed in the measurement between $B_{\parallel} = 0$ T and 3T; however, finite magnetization develops above 3T, the same range of magnetic fields where the resistivity peak develops (see Supplementary Fig. 2). We thus associate the resistivity peak with the formation of an isospin-polarized state at finite magnetic field. This is consistent with the hypothesis that the anomalous resistivity peak that develops under an in-plane magnetic field indeed marks the boundary between a polarized and an unpolarized phase, similar to the behaviour under an out-of-plane magnetic field in this density regime^{3,24,27,28}.

Entropically driven transition at finite temperature

The apparent duality between B_{\parallel} and T-dependent transport is suggestive of an entropically driven transition at finite temperature. In this scenario, the unpolarized Fermi liquid state has lower ground-state

energy than the IF₃ phase near v = -1, but the fluctuating moments of the IF₃ state make it entropically favourable at elevated temperature. The characteristic temperature scale at which these moments begin to fluctuate strongly, giving rise to a large isospin entropy, is given by the stiffness of the collective excitations of the spin, valley and carbon sublattice degrees of freedom³³, which numerical calculations find to be in the few-meV range^{4,5,34,35}. Combined with the expectation that ground-state energies differ by similar energy scales, an entropically driven transition in the approximately 10-K regime is highly plausible. This is analogous to the well known Pomeranchuk effect in ³He, where the liquid transforms into a solid upon raising the temperature. In our system, the role of the liquid phase is played by the unpolarized Fermi liquid, whereas the high-temperature 'solid' analogue is the high-temperature extension of the IF₃ phase, which—though it may have only negligible net magnetization—is distinguished by the presence of local, strongly fluctuating magnetic moments.

The connection between low-T, high- B_{\parallel} and high- TB_{\parallel} = 0 phases is confirmed by variable temperature measurements of the longitudinal resistivity ρ_{xx} , shown in Fig. 3a, where we plot ρ_{xx} as a function of v_0 and total magnetic field B_{tot} oriented at an angle of 9.1° relative to the sample plane, measured at 5 K and 10 K. At the higher temperatures, the resistivity peak separating the high-temperature extensions of the IU and IF₃ phases is visible at $B_{\text{tot}} = 0$ T, and is observed to move towards neutrality as a function of B_{tot} (see also Extended Data Fig. 7) precisely the expected behaviour if the two high-temperature phases differ in their spin polarization or magnetic susceptibilities. As shown in Fig. 3b, the resistivity peak can be used to map the boundary between the isospin-symmetric phase prevailing at lower B, T and $|v_0|$, and a state of finite spin susceptibility at higher temperatures, as shown in Fig. 3b. We note that a similar behaviour of the phase boundary is both expected and observed near $v_0 = +1$, even when the ground state is the IF₃ phase, as in device 2 (Extended Data Fig. 8).

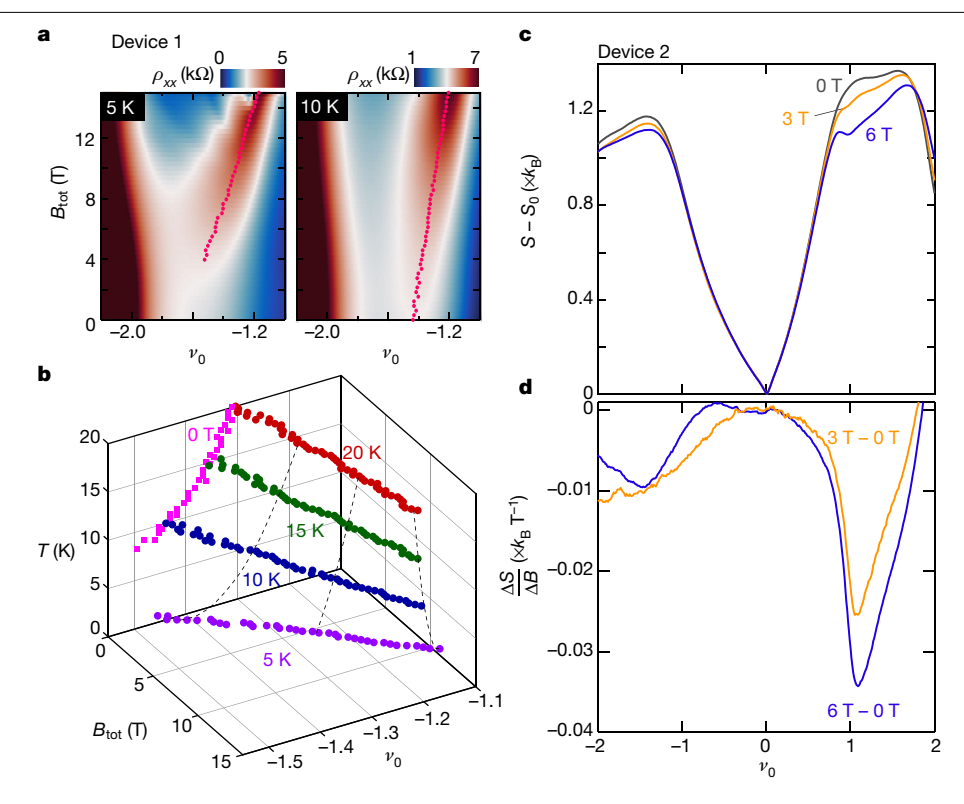


Fig. 3 | Isospin Pomeranchuk effect and spin entropy. a, ρ_{xx} as a function of v_0 and B_{tot} oriented at an angle of 9.1° relative to the sample plane, measured at 5 K and 10 K in device 1. Pink circles correspond to ρ_{xx} peak positions. ${\bf b}$, The position of resistive peaks v_{peak} as a function of B_{tot} and T. The dashed curves are polynomial fits to the dots at B_{\parallel} = 5, 10 and 15 T. c, Entropy per superlattice unit

cell measured relative to the charge neutrality point, $S - S_0$. Entropy is derived from the finite difference between $\mu(v_0)$ data measured at 4.2 K and 12 K for B_{\perp} = 0, 3 and 6 T. $\mathbf{d}, \Delta S/\Delta B$ as a function of v_0 at T = 8.1 K, calculated from (S(6T) - S(0T))/6T (blue) and (S(3T) - S(0T))/3T (yellow).

Under an out-of-plane magnetic field, B_{\perp} , the low-temperature magnetic transition appears to be first order for at least some range of v (refs. 3,24), showing sharp jumps in experimental observables and hysteretic behaviour. A key prediction of the first-order scenario is a jump in the entropy between the IU and IF₃ phases arising from disordering of isospins at finite temperature. We measured the total electronic entropy from the response of u to changes in T via the Maxwell relation $(\partial \mu/\partial T)_y = -(\partial S/\partial v)_T$, approximating $\partial \mu/\partial T$ from the finite difference of u measurements at 4.2 K and 12 K. Figure 3c shows the experimentally determined entropy, measured relative to the entropy at the charge neutrality point, $S(v_0) - S_0$. The uncertainty estimated from the integration process is shown in Supplementary Fig. 6. The entropy rises upon both electron or hole doping, reaching $\Delta S/k_{\rm B} \approx 1$ ($k_{\rm B}$, Boltzmann constant) per superlattice unit cell near $v_0 = \pm 1$, where it levels off or even decreases. However, we observed no jump, in effect ruling out a first-order transition. This is consistent with the absence of sharp features in either temperature-dependent or B_{\parallel} -dependent transport measurements, suggesting that the transition is either of higher order or simply a crossover.

Nevertheless, the existence of disordered isospins in the high-temperature IF₃ phases is supported by the measured behaviour of the entropy as a function of in-plane magnetic field. As shown in Fig. 3d, ΔS decreases as a function of B_{\parallel} for $v_{0\parallel} \gtrsim 1$ and $v_0 \lesssim -1$, corresponding to the high-temperature IF₃ phases, but gives no experimentally detectable change in the IU phase. At temperatures of the order of the spin stiffness, the IF₃ phase is strongly fluctuating, leading to a spin-dependent $S \approx k_B \ln 2$ contribution to the entropy. This entropy can be suppressed by a Zeeman energy $E_Z \approx k_B T$. We thus expect $\Delta S/$ $\Delta B \approx \mu_B / T \approx 0.08 k_B T^{-1} (\mu_B$, Bohr magneton) for the T = 8 K temperature of our measurement. We indeed observe an entropy suppression of this scale for $v_0 \gtrsim 1$, suggesting that the spin stiffness is indeed small, and supporting the picture of a spin-entropy-driven Pomeranchuk effect. A smaller entropy suppression is observed for $v_0 \le -1$. This could arise from a larger spin stiffness in the IF₃ phase at hole doping. The discrepancy between electron and hole doping highlights the quantitative importance of the particle-hole asymmetry of the underlying single-particle wavefunctions, a problem that recent theoretical literature has only begun to address^{4,5,34-37}.

Electronic compressibility at high temperature

Our observation of an entropically driven transition suggests that soft neutral excitations of the electron system probably have a key role in the physics of flat-band moiré systems. Although long-range magnetic order may appear only at low temperature or in the presence of a magnetic field, much of the phase diagram is dominated by the presence of large, strongly fluctuating local moments. A measurement of the compressibility $\partial \mu / \partial v_0$ as a function of density for a range of temperatures between 4.2 K and 96 K (Fig. 4) shows a sequence of nearly commensurate, asymmetric peaks (see also Extended Data Fig. 9). These peaks have been interpreted 25,32,38 as indicating Fermi surface reconstruction, owing to a cascade of isospin-symmetry-breaking transitions. Notably, however, our measurements show that the peaks in $\partial \mu / \partial v_0$ survive even at temperatures well above the scale of the spin stiffness, where no magnetic order is found. The compressibility features themselves disappear only at $T \approx 100$ K, comparable to the scale of the Coulomb interaction². We emphasize that in our thermodynamic measurements, the development of finite magnetization is a detectable but subtle effect that does not qualitatively impact the structure of the chemical potential (see Extended Data Fig. 6). It therefore seems probable that the peaks in $\partial \mu / \partial v_0$ mark the formation of local isospin moments, correlated only on length scales comparable to the moiré wavelength.

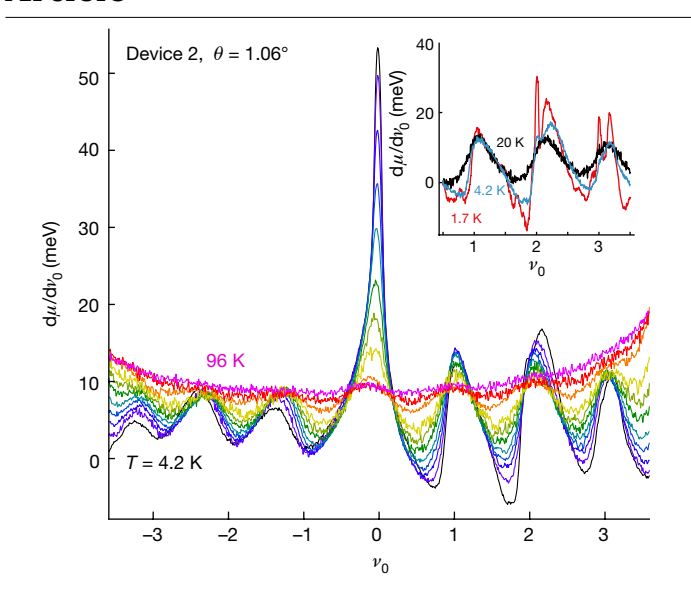


Fig. 4 | **Temperature dependence of the inverse electronic compressibility** $d\mu/d\nu_0$. The data are acquired at 4.2, 8, 12, 16, 20, 26, 32, 40, 59, 76 and 96 K. Approximately commensurate oscillations appear at $T \lesssim 100$ K, the approximate scale of the Coulomb interactions. Thermodynamic gaps at $\nu_0 = 2$, 3 appear only below 4.2 K, as shown in the inset, which gives $d\mu/d\nu_0$ traces for 20 K, 4.2 K, and 1.7 K in black, cyan, and red respectively.

The presence of strongly fluctuating isospin moments in much of the phase diagram should have a profound effect on the physics of twisted bilayer graphene. The small stiffness implied by our measurements may serve as an upper bound on the superconducting critical temperature, T_c , in regions of the phase diagram where isospin order is observed, either because the isospin fluctuations act as pair-breakers, or because the pairing mechanism itself requires isospin order. For example, isospin ordering is a prerequisite for the existence of skyrmion textures recently proposed to have a role in the superconductivity observed in twisted bilayer graphene⁵.

Thermal disordering of the internal degrees of freedom is also expected to strongly scatter electrons at these temperatures. Some portion, if not the majority, of the large high-temperature resistivity in flat-band moiré systems probably arises from such scattering. This appears consistent with the experimentally observed ubiquity of both the ferromagnetism across the flat band 25,38 and also the large resistivity at intermediate temperatures 6,7 . In addition, the 'superconducting-like' transition observed in many moiré systems, in which the resistivity rises rapidly at temperatures of a few kelvin, probably indicates the onset (at high temperatures) of this fluctuation-moment phase. The precise temperature dependence of the resistivity is not expected to be universal, depending on the details of the collective excitations and their coupling to the itinerant conduction electrons. This is consistent with experimental observation of the strong ν_0 dependence of $\rho_{xx}(T)$ (see Supplementary Fig. 7).

Online content

Any methods, additional references, Nature Research reporting summaries, source data, extended data, supplementary information, acknowledgements, peer review information; details of author contributions and competing interests; and statements of data and code availability are available at https://doi.org/10.1038/s41586-021-03409-2.

1. Pomeranchuk, I. On the theory of liquid 3-He. Zh. Eksp. Teor. Fiz **20**, 919–926 (1950).

- Andrei, E. Y. & MacDonald, A. H. Graphene bilayers with a twist. Nat. Mater. 19, 1265–1275 (2020); correction https://doi.org/10.1038/s41563-020-00917-w (2021).
- Lu, X. et al. Superconductors, orbital magnets and correlated states in magic-angle bilayer graphene. Nature 574, 653–657 (2019).
- Wu, F. & Sarma, S. D. Collective excitations of quantum anomalous Hall ferromagnets in twisted bilayer graphene. Phys. Rev. Lett. 124, 046403 (2020).
- Khalaf, E., Chatterjee, S., Bultinck, N., Zaletel, M. P. & Vishwanath, A. Charged skyrmions and topological origin of superconductivity in magic-angle graphene. Preprint at https:// arxiv.org/abs/2004.00638 (2020).
- Polshyn, H. et al. Large linear-in-temperature resistivity in twisted bilayer graphene. Nat. Phys. 15, 1011–1016 (2019).
- Cao, Y. et al. Strange metal in magic-angle graphene with near Planckian dissipation. Phys. Rev. Lett. 124, 076801 (2020).
- He, M. et al. Tunable correlation-driven symmetry breaking in twisted double bilayer graphene. Nat. Phys. 17, 26–30 (2021).
- Cao, Y. et al. Unconventional superconductivity in magic-angle graphene superlattices. Nature 556, 43–50 (2018).
- Yankowitz, M. et al. Tuning superconductivity in twisted bilayer graphene. Science 363, 1059–1064 (2019).
- Bistritzer, R. & MacDonald, A. H. Moiré bands in twisted double-layer graphene. Proc. Natl Acad. Sci. USA 108, 12233–12237 (2011).
- Cao, Y. et al. Correlated insulator behaviour at half-filling in magic-angle graphene superlattices. Nature 556, 80–84 (2018).
- Sharpe, A. L. et al. Emergent ferromagnetism near three-quarters filling in twisted bilayer graphene. Science 365, 605–608 (2019).
- Saito, Y., Ge, J., Watanabe, K., Taniguchi, T. & Young, A. F. Independent superconductors and correlated insulators in twisted bilayer graphene. Nat. Phys. 16, 926–930 (2020).
- Stepanov, P. et al. Untying the insulating and superconducting orders in magic-angle graphene. Nature 583, 375–378 (2020).
- Arora, H. S. et al. Superconductivity in metallic twisted bilayer graphene stabilized by WSe., Nature 583, 379–384 (2020).
- Serlin, M. et al. Intrinsic quantized anomalous Hall effect in a moiré heterostructure. Science 367, 900-903 (2020).
- Tschirhart, C. L. et al. Imaging orbital ferromagnetism in a moiré Chern insulator. Preprint at https://arxiv.org/abs/2006.08053 (2020).
- Dodaro, J. F., Kivelson, S. A., Schattner, Y., Sun, X. Q. & Wang, C. Phases of a phenomenological model of twisted bilayer graphene. *Phys. Rev. B* 98, 075154 (2018).
- Wu, F., MacDonald, A. H. & Martin, I. Theory of phonon-mediated superconductivity in twisted bilayer graphene. *Phys. Rev. Lett.* 121, 257001 (2018).
- Lian, B., Wang, Z. & Bernevig, B. A. Twisted bilayer graphene: a phonon-driven superconductor. Phys. Rev. Lett. 122, 257002 (2019).
- 22. Martin, I. Moiré superconductivity. Ann. Phys. 417, 168118 (2020).
- Wu, F., Hwang, E. & Das Sarma, S. Phonon-induced giant linear-in-T resistivity in magic-angle twisted bilayer graphene: ordinary strangeness and exotic superconductivity. Phys. Rev. B 99, 165112 (2019).
- Saito, Y. et al. Hofstadter subband ferromagnetism and symmetry-broken Chern insulators in twisted bilayer graphene. Nat. Phys. https://doi.org/s41567-020-01129-4 (2021).
- Zondiner, U. et al. Cascade of phase transitions and Dirac revivals in magic-angle graphene. Nature 582, 203–208 (2020).
- Xie, M. & MacDonald, A. H. Weak-field Hall resistivity and spin/valley flavor-symmetry breaking in MAtBG. Preprint at https://arxiv.org/abs/2010.07928 (2020).
- Wu, S., Zhang, Z., Watanabe, K., Taniguchi, T. & Andrei, E. Y. Chern insulators and topological flat-bands in magic-angle twisted bilayer graphene. Preprint at https://arxiv. org/abs/2007.03735 (2020).
- Nuckolls, K. P. et al. Strongly correlated Chern insulators in magic-angle twisted bilayer graphene. Nature 588, 610–615 (2020).
- Liu, X. et al. Tuning electron correlation in magic-angle twisted bilayer graphene using Coulomb screening. Preprint at https://arxiv.org/abs/2003.11072 (2020).
- Lee, K. et al. Chemical potential and quantum Hall ferromagnetism in bilayer graphene. Science 345, 58–61 (2014).
- Yang, F. et al. Experimental determination of the energy per particle in partially filled Landau levels. Preprint at https://arxiv.org/abs/2008.05466 (2020).
- Park, J. M., Cao, Y., Watanabe, K., Taniguchi, T. & Jarillo-Herrero, P. Flavour Hund's coupling, Chern gaps and charge diffusivity in moiré graphene. Nature https://www. nature.com/articles/10.1038/s41586-021-03366-w (2021).
- Bultinck, N. et al. Ground state and hidden symmetry of magic-angle graphene at even integer filling. Phys. Rev. X 10, 031034 (2020).
- Khalaf, E., Bultinck, N., Vishwanath, A. & Zaletel, M. P. Soft modes in magic-angle twisted bilayer graphene. Preprint at https://arxiv.org/abs/2009.14827 (2020).
- Kumar, A., Xie, M. & MacDonald, A. H. Lattice collective modes from a continuum model of magic-angle twisted bilayer graphene. Preprint at https://arxiv.org/abs/2010.05946 (2020).
- Bernevig, B. et al. TBG V. Exact analytic many-body excitations in twisted bilayer graphene Coulomb Hamiltonians: charge gap, Goldstone modes and absence of Cooper pairing. Preprint at https://arxiv.org/abs/2009.14200 (2020).
- Vafek, O. & Kang, J. Renormalization group study of hidden symmetry in twisted bilayer graphene with Coulomb interactions. Phys. Rev. Lett. 125, 257602 (2020).
- Wong, D. et al. Cascade of electronic transitions in magic-angle twisted bilayer graphene Nature 582, 198–202 (2020).

Publisher's note Springer Nature remains neutral with regard to jurisdictional claims in published maps and institutional affiliations.

© The Author(s), under exclusive licence to Springer Nature Limited 2021

Methods

Device fabrication and transport measurements

In this study, we used two twisted bilayer graphene (tBLG) devices: device 1 (1.12°) and device 2 (1.06°). Both devices were fabricated using a 'cut-and-stack' technique, described in ref. 14 . Device 1 is the same as device 5 in ref. 14 and the device studied in ref. 24 . Device 2 is the same as the device used in ref. 29 . Prior to stacking, we first cut the graphene into two pieces using atomic force microscopy to prevent unintentional strain in tearing the graphene. We used a poly(bisphenol A carbonate)/polydimethylsiloxane (PC/PDMS) stamp mounted on a glass slide for stacking tBLG heterostructures. The final structure of devices 1 and 2 are hBN(40 nm)–tBLG–hBN(40 nm)–graphite and graphite–hBN(30 nm)–tBLG–hBN(30 nm)–graphite, respectively, as shown in Extended Data Fig. 1 (hBN, hexagonal boron nitride). Electrical connections to the tBLG were made by CHF $_3$ /O $_3$ etching and deposition of the Cr/Pd/Au (2/15/180 nm) metal edge contacts for device 1 and Cr/Au (2/100 nm) metal edge contacts for device 2 (ref. 39).

Transport data in Fig. 1a–d (0.5, 2.5, 4.5 K) were acquired with device 1 in a top-loading cryogen-free dilution refrigerator with a nominal base temperature of 10 mK, using a probe with heavy radiofrequency filtering at an excitation current of 2 nA at a frequency of 17.777 Hz. Data in Fig. 2a–c were acquired in a different probe without filtering at an excitation current of 10 nA at a frequency of 278 Hz. Data in Fig. 1d (8 K and 20 K), and Figs. 2d, 3a were acquired using a wet, sample-in-vapour variable-temperature system without filtering at an excitation current of 10 nA at a frequency of 278 Hz.

We measure the geometric capacitance in device 1 from the Hall density near the charge neutrality point to be $c_{\rm g}=58.2\pm0.3~\rm nF~cm^{-2}$. Separate measurements using quantum oscillations give comparable results, $c_{\rm g}=58.5\pm0.1~\rm nF~cm^{-2}$. The twist angle θ is determined from the values of the charge carrier density n at which the insulating states ($v_0=\pm2$) at $n_{v_0=\pm2}$ are observed, following $n_{v_0=\pm2}=\pm4\theta^2/\sqrt{3}~a^2$, where $a=0.246~\rm nm$ is the lattice constant of graphene. From these measurements, $v_0=A_{\rm u.c.}c_{\rm g}/e(v_{\rm g}-v_{\rm g}^0)$, where $v_{\rm g}$ is the gate voltage, $v_{\rm g}^0$ is the gate voltage corresponding to charge neutrality, e is the electron charge and $A_{\rm u.c.}c_{\rm g}/e=0.5026~\rm V^{-1}$. Here $A_{\rm u.c.}$ is the area of the unit cell (u.c.).

Thermodynamic determination of μ , M and S

The entropy (S) and the magnetization (M) are determined by measuring temperature-dependent and in-plane magnetic-field-dependent chemical potential μ and making use of the Maxwell relations:

$$\left(\frac{\partial S}{\partial \nu}\right)_{T} = -\left(\frac{\partial \mu}{\partial T}\right)_{\nu} \quad \text{and} \quad (1)$$

$$\left(\frac{\partial M}{\partial \nu}\right)_{B} = -\left(\frac{\partial \mu}{\partial B}\right)_{\nu},$$

where v is the filling factor. S and M can then be determined by integrating the measured right-hand sides of equation (1) with respect to v. We perform the thermodynamic measurements on device 2, which consists of a 1.06°-angle tBLG separated by a 3-nm BN spacer from a Bernal-stacked bilayer flake that is separately contacted (Extended Data Fig. 1b). Transport data from this device was described in ref. ²⁹. To determine the chemical potential, we use the measurement technique described in ref. 31. In this technique, an excitation current (5-50 nA) with frequency $f_1 = 321 \text{ Hz}$ is used to measure the four-terminal resistance $R_{\rm BLG}$ of the Bernal bilayer graphene, and a second frequency f_2 = 123 Hz is used to modulate the top-gate voltage (V_{tg}) resulting in a measurable response at frequency $f_1 - f_2$ proportional to dR_{BLG}/dV_{tg} ; crucially, this response vanishes at a resistivity extremum such as the charge neutrality point. A feedback loop is then used to maintain dR_{BLG} $dV_{tg} = 0$ as the bottom gate is changed by applying a feedback voltage to the twisted bilayer. The output voltage of this feedback loop is then

equal to μ/e . In all measurements, the displacement field of the Bernal bilayer graphene is maintained at D = 14 mV nm⁻¹.

Strictly speaking, our technique measures $\mu_{\rm tBLG}(\nu) - \mu_{\rm bBLG}^{\rm CNP}$, the difference in chemical potential between the twisted bilayer and the charge-neutral Bernal bilayer detector. Although the change in $\mu_{\rm bBLG}^{\rm CNP}$ with temperature and magnetic field is small, so are differences in $\mu_{\rm tBLG}(\nu)$. To fix the possible offset between curves measured under different conditions, we set $d\mu/dB_{\parallel}$ and $d\mu/dT$ to be zero at $\nu_0=0$. These curves are then integrated from $\nu_0=0$ filling factors. We thus measure $S-S_0$ and $M_{\parallel}-M_{\parallel,0}$ —that is, the changes in S_{\parallel} and M_{\parallel} relative to their values at charge neutrality:

$$S(v_0) - S_0 = \int_0^{v_0} \left(\frac{\partial S}{\partial v} \right) dv - v_0 \frac{\partial S}{\partial v} \bigg|_{v_0 = 0} \quad \text{and}$$

$$M_{\parallel}(v_0) - M_{\parallel,0} = \int_0^{v_0} \left(\frac{\partial M}{\partial v} \right) dv - v_0 \frac{\partial M}{\partial v} \bigg|_{v_0 = 0}.$$
(2)

In the case of M_{\parallel} , we expect that $M_{\parallel,0}$ vanishes, owing to the absence of in-plane B dependence of measured quantities as well as from the flat behaviour of dM_{\parallel}/dv in that region. However, in the case of S, charge neutrality may well develop a large entropy both from excited quasiparticles at high temperature or from modes associated with the breaking of additional symmetries in the charge neutral state. However, we note that for the purposes of correlating the behaviour of transport near $v=\pm 1$ with the state surrounding charge neutrality, $S-S_0$ is the relevant quantity.

Thermodynamic model

To describe the phase transition between the IU to the IF₃ phases, we write their free energy per moiré unit cell as:

$$f_i(v, T) = e_i + \frac{1}{2} \left(\frac{1}{\kappa_i} + \frac{e^2}{c_g} \right) v^2 + \mu_i v - \frac{1}{2} \gamma_i T^2 - s_i T,$$
 (3)

where i=1,2 corresponds to the IU and IF₃ phases, respectively, e is the elementary charge, e_i is an offset energy, c_g is the geometric capacitance to the gate per moiré unit cell, μ_i is an offset chemical potential, γ_i is the specific heat coefficient (both phases are assumed to be metallic, despite the fact that the IF₃ phase has large, fluctuating magnetic moments), and κ_i is the compressibility (or quantum capacitance). s_i is a temperature-independent contribution of the entropy. The IU phase is a Fermi liquid the entropy of which is proportional to temperature, hence $s_1 = 0$. In the IF₃ phase, the fluctuating moments give a contribution $s_2 > 0$ to the entropy at temperatures exceeding spin stiffness.

Because the experiment is carried out at a constant gate voltage, the phase transition (assumed to be of first order in the absence of disorder) occurs when the Landau grand potential $\Omega_i(v_g,T)=f_i(v,T)-ev_gv$ of the two phases are equal. We minimize the grand potentials of each phase with respect to v, and express the grand potentials in terms of the reference filling factor, $v_0 \equiv \frac{1}{e} c_g v_g$. The transition line in the (v_0,T) plane is then given by the condition:

$$\Omega_2 - \Omega_1 = \Delta \tilde{e}(\nu_0) - \frac{1}{2} \Delta \gamma T^2 - T \Delta s = 0, \tag{4}$$

where $\Delta \widetilde{e}(\nu_0) \approx e_2 - e_1 - \frac{1}{2} \left(\frac{1}{\kappa_2} - \frac{1}{\kappa_1} \right) \nu_0^2 + (\mu_2 - \mu_1) \nu_0$, $\Delta \gamma = \gamma_2 - \gamma_1$, and $\Delta s = s_2 - s_1$. Here we have used the fact that in our setup, $\frac{e^2}{c_g} \gg \frac{1}{\kappa_{1,2}}$, and we have neglected terms that are suppressed by factors of $\frac{c_g}{e^2 \kappa_{1,2}}$. At sufficiently low temperature compared to the bandwidth (estimated to be of the order of 200–300 K), the quadratic term in T is much smaller than the linear term, giving a transition at:

$$T^* = \frac{\Delta \widetilde{e}(\nu_0)}{\Delta s}.$$
 (5)

To determine the entropy Δs from the experiment, we need an estimate of $\Delta e(v_0)$. This can be obtained by examining the magnetic field needed to trigger the transition from the IU to the IF₃ phase at low temperature (below the spin stiffness in the IF₃ phase). We consider an in-plane field, assuming that it acts primarily through the Zeeman effect. The magnetic field induces an additional term in the grand potentials equal to $-\int_{0}^{B} m_{i}(B') dB'$, where $m_{i}(B)$ is the magnetic moment per moiré unit cell. At sufficiently low temperature, where the excess magnetic entropy s₂ of the IF₃ phase is quenched, this phase is spin polarized, and its magnetization is nearly field-independent. To the magnetic moment in this phase, we assume that one isospin flavour whose spin is antiparallel to the Zeeman field is completely empty (that is, this flavour has a filling of one hole away from charge neutrality), whereas the other three flavours are equally populated²⁵. These considerations give a magnetic moment of $m_2 = \mu_B(4 + \nu_0)/3$ in the IF₃ phase. By contrast, the IU phase has no magnetic moment at B = 0. Because the IU phase is a Fermi liquid, its magnetization is proportional to the ratio between the Zeeman energy and the bandwidth, and is much smaller than that of the IF₃ phase. We therefore neglect the magnetization of the IU phase, $m_1 \approx 0$. The field-driven transition at low temperature occurs when:

$$\Delta \tilde{e}(v_0) - \mu_B \frac{4 + v_0}{3} B^* = 0.$$
 (6)

Combining equations (5) and (6) gives:

$$\Delta s = \frac{E_Z^*(\nu_0)}{T^*(\nu_0)} \frac{4 + \nu_0}{3} \tag{7}$$

We plot the expected entropy in Extended Data Fig. 10.

Data availability

All data that support the plots within this paper and other findings of this study are available from the corresponding author upon reasonable request. Source data are provided with this paper.

 Wang, L. et al. One-dimensional electrical contact to a two-dimensional material. Science 342, 614–617 (2013).

Acknowledgements We acknowledge discussions with S. Kivelson, A. Macdonald, B. Spivak and M. Zaletel, as well as experimental assistance from H. Polshyn and C. Tschirhart. Y.S. acknowledges the support of the Elings Prize Fellowship from the California NanoSystems Institute at University of California, Santa Barbara. K.W. and T.T. acknowledge support from the Elemental Strategy Initiative conducted by the MEXT, Japan and the CREST (JPMJCR15F3), JST. Transport and fabrication experiments at UCSB were supported by the ARO under MURI W911NF-16-1-O361. Thermodynamic measurements were supported by the National Science Foundation under DMR-1654186. A.F.Y. acknowledges the support of the David and Lucille Packard Foundation under award 2016-65145. E.B. was supported by the European Research Council (ERC) under grant HQMAT (grant number 817799), and by the US-Israel Binational Science Foundation (BSF) under the NSF-BSF DMR programme (grant number DMR-1608055). X.L. and J.I.A.L. are supported by Brown University.

Author contributions Y.S., J.G. and X.L. fabricated tBLG devices. Y.S. and F.Y. performed the measurements. Y.S., F.Y. and A.F.Y. analysed the data. A.F.Y. and E.B. constructed the thermodynamic model. Y.S., F.Y., E.B. and A.F.Y. wrote the paper with input from J.I.A.L. T.T. and K.W. grew the hBN crystals.

Competing interests The authors declare no competing interests.

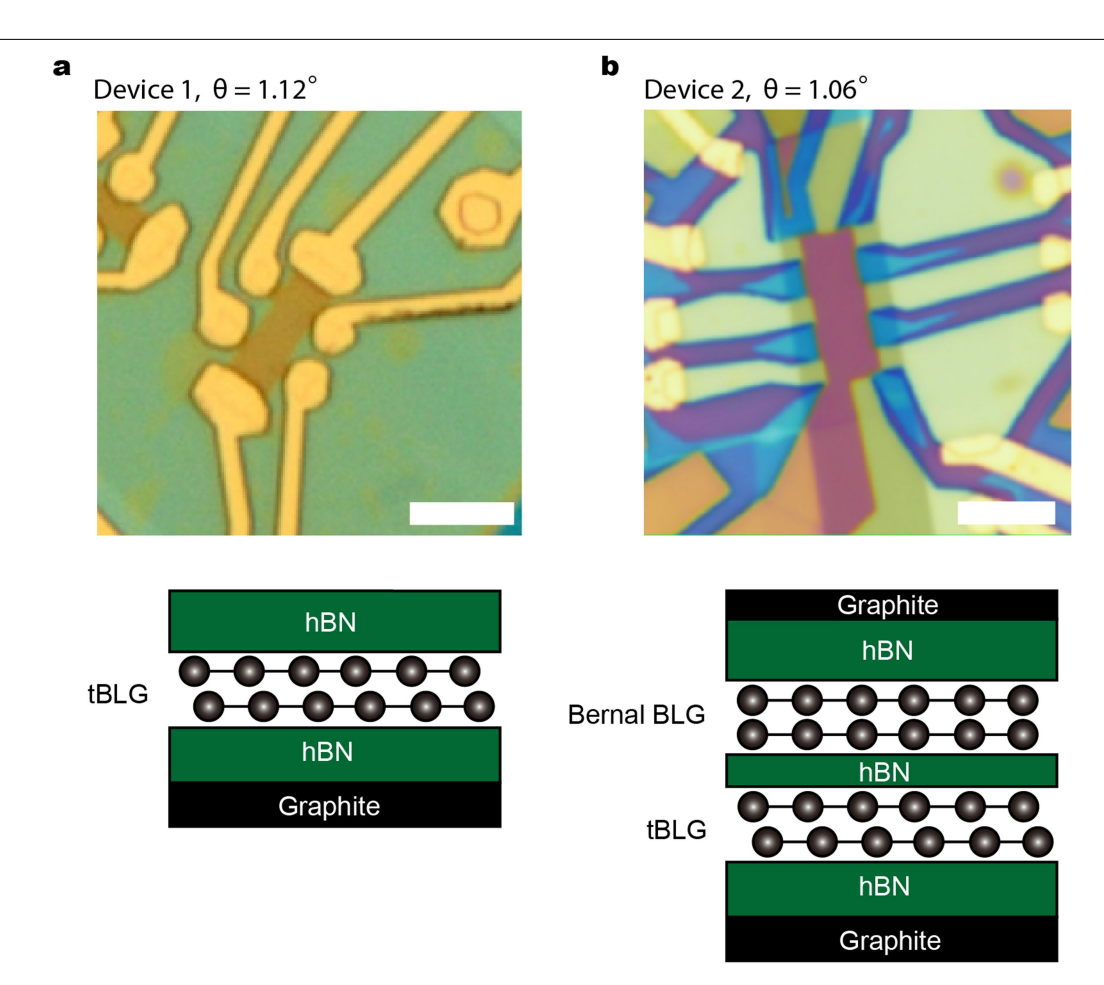
Additional information

Supplementary information The online version contains supplementary material available at https://doi.org/10.1038/s41586-021-03409-2.

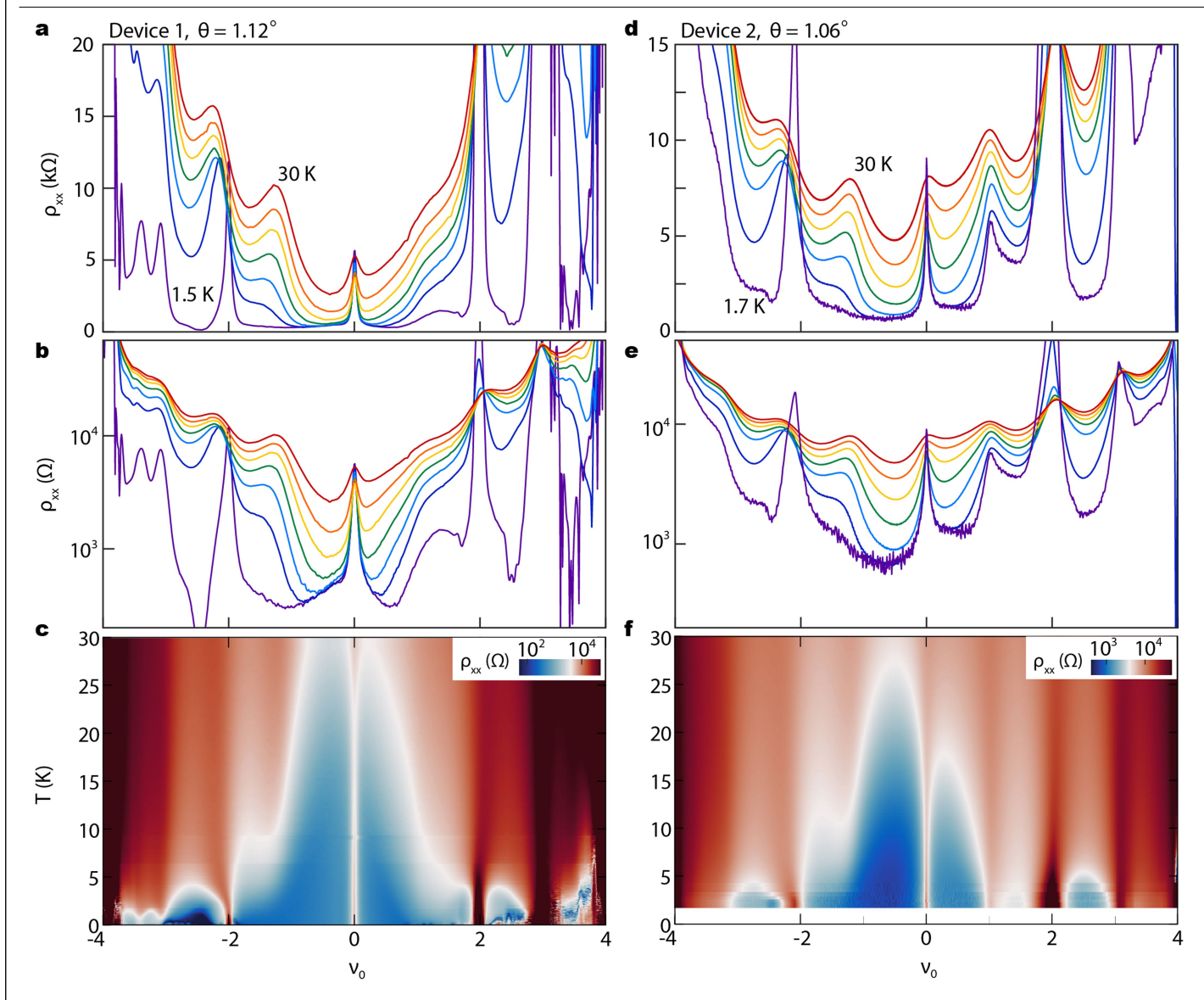
Correspondence and requests for materials should be addressed to A.F.Y.

Peer review information *Nature* thanks Xuan Gao, Emanuel Tutuc and the other, anonymous, reviewer(s) for their contribution to the peer review of this work. Peer reviewer reports are available.

Reprints and permissions information is available at http://www.nature.com/reprints.

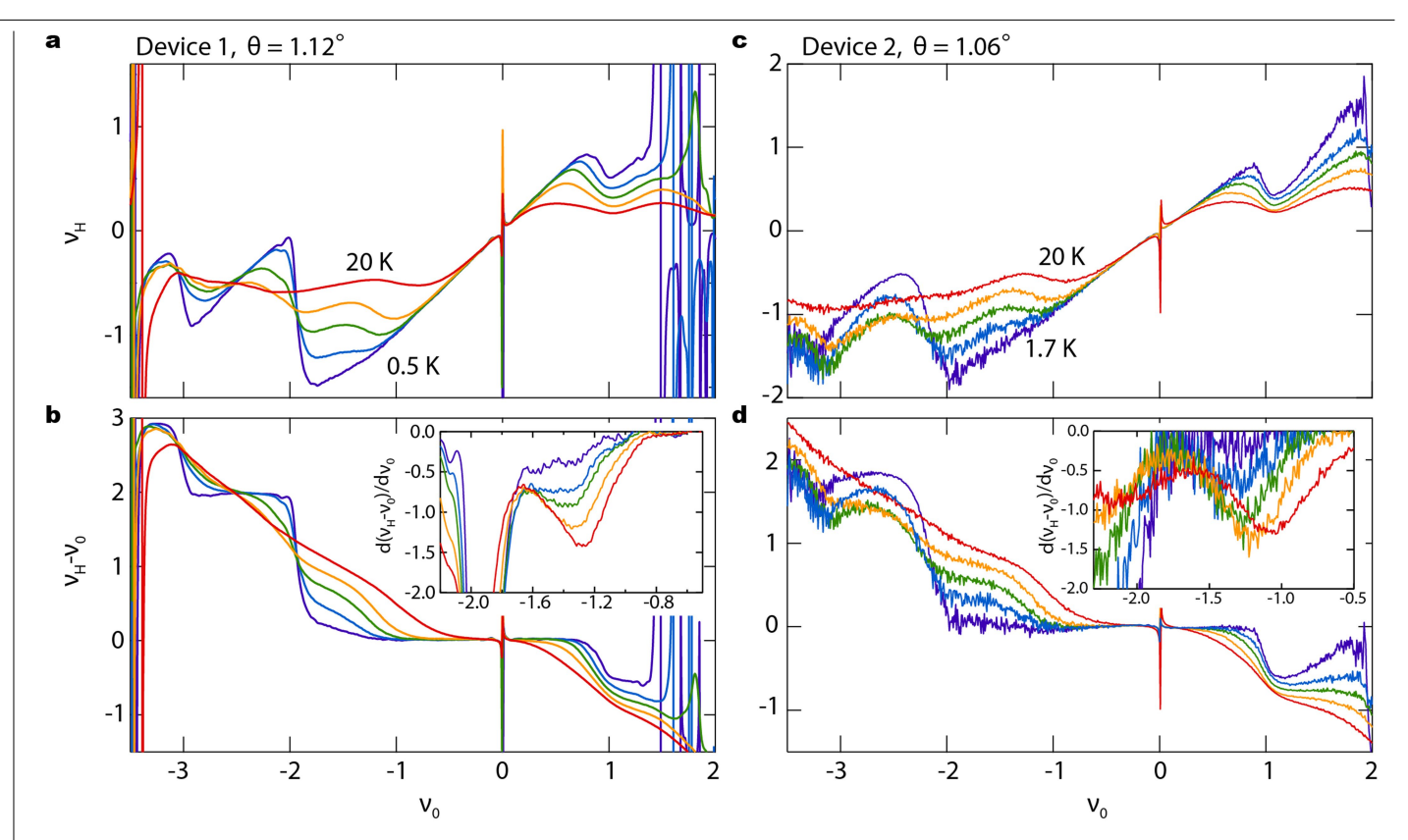


 $\textbf{Extended Data Fig. 1} \\ \textbf{tBLG devices. a, b}, \\ \textbf{Top, optical images of device 1(a)} \\ \textbf{and device 2(b)}. \\ \textbf{Scale bars correspond to 5} \\ \mu \textbf{m. Bottom, schematic of the tBLG} \\ \textbf{heterostructures for device 1(a)} \\ \textbf{and device 2(b)}. \\ \textbf{And device 2(b)$



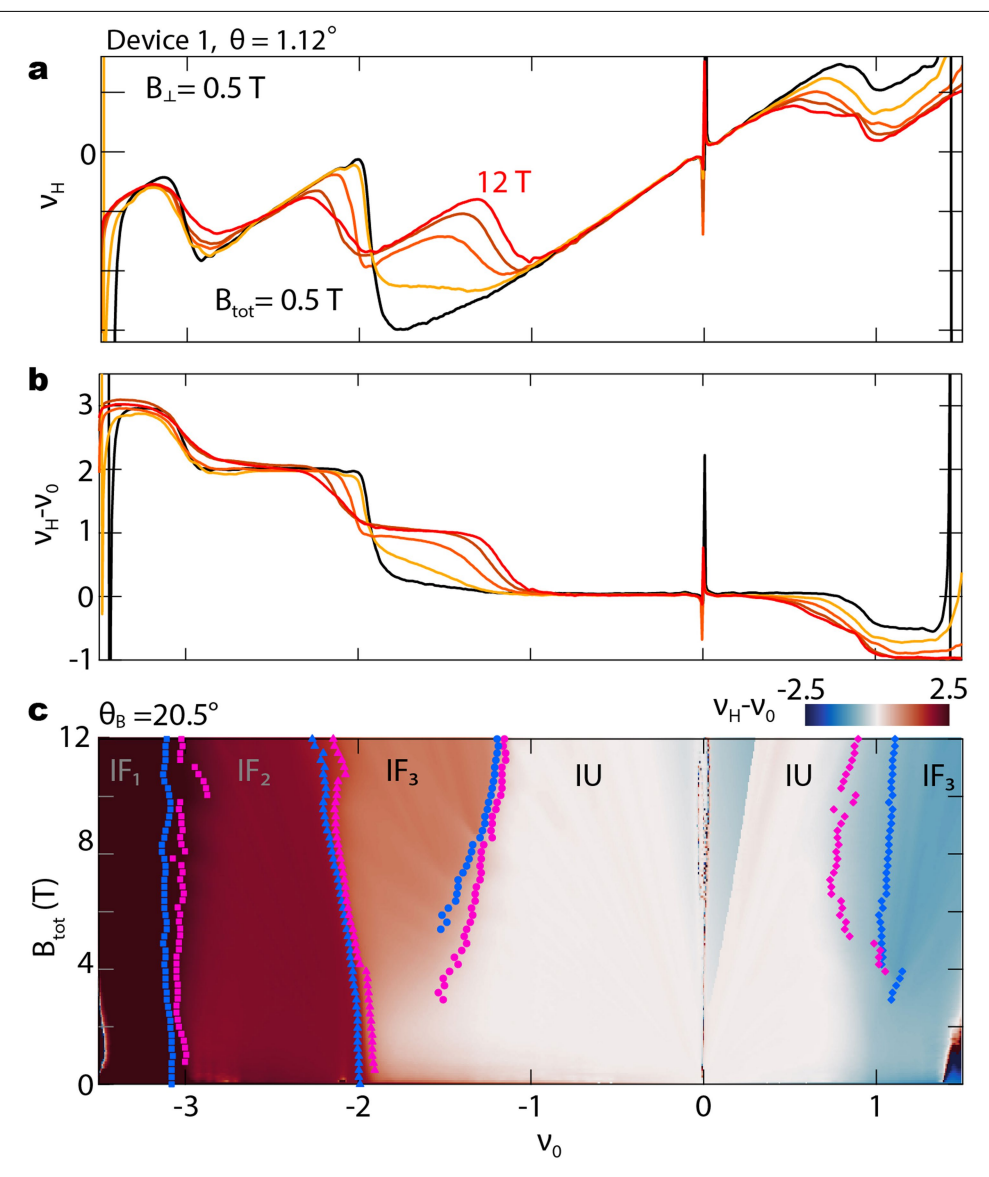
Extended Data Fig. 2 | **Temperature dependence of the resistivity** ρ_{xx} , \mathbf{a} , \mathbf{b} , \mathbf{d} , \mathbf{e} , ρ_{xx} as a function of the nominal filling factor v_0 at various temperatures up to 30 K in device 1 (\mathbf{a} , linear scale; \mathbf{b} , logarithmic scale) and device 2 (\mathbf{d} , linear scale; \mathbf{e} , logarithmic scale). The traces in \mathbf{a} , \mathbf{b} are measured at

T=1.5,5,8,12,17,22 and 30 K and the traces in **d**, **e** are measured at T=1.7,5,10, 15,20,25 and 30 K. **c**, **f**, Two-dimensional map of ρ_{xx} as a function of ν_0 and T in device 1 (**c**) and device 2 (**f**).



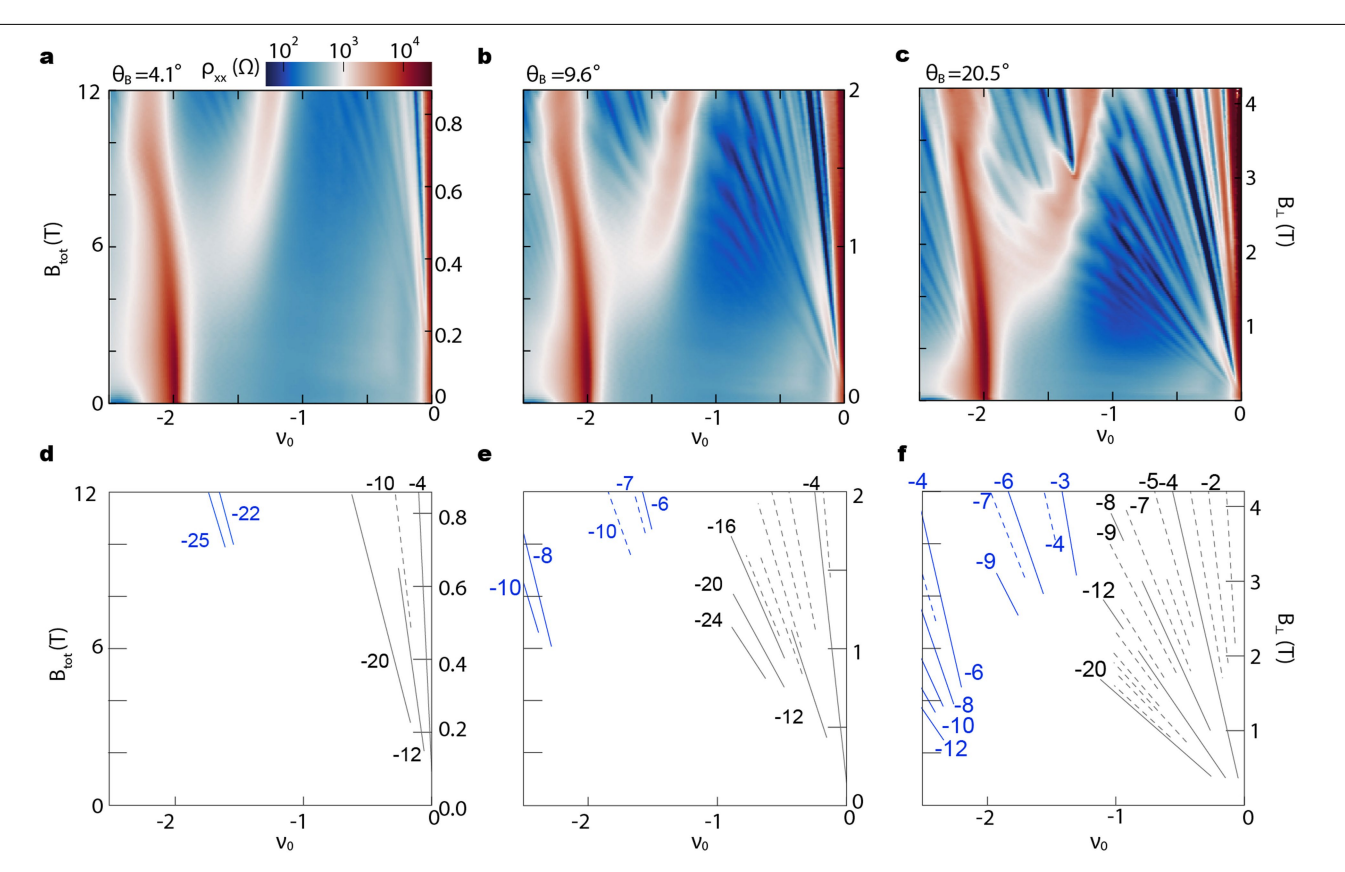
Extended Data Fig. 3 | **Temperature dependence of the Hall density behaviour. a, c,** The Hall density $v_{\rm H}$ expressed in electrons per superlattice unit cell as a function of v_0 up to 20 K at a fixed B_{\perp} = 0.5 T. The data of device 1 are measured with T = 0.5, 2.5, 4.5, 8 and 20 K (**a**) and the data of device 2 are measured with T = 1.7, 4.3, 6, 10 and 20 K (**c**). **b, d**, Subtracted Hall density $v_{\rm H}$ – v_0

as a function of v_0 at each temperature in device 1 (**b**) and device 2 (**d**). Insets, $d(v_H - v_0)/dv_0$ as a function of v_0 at each temperature around $v_0 = -1$. $d(v_H - v_0)/dv_0$ is calculated from $v_H - v_0$ using a 20-point moving average (**b**) and a 40-point moving average (**d**) in v_0 .



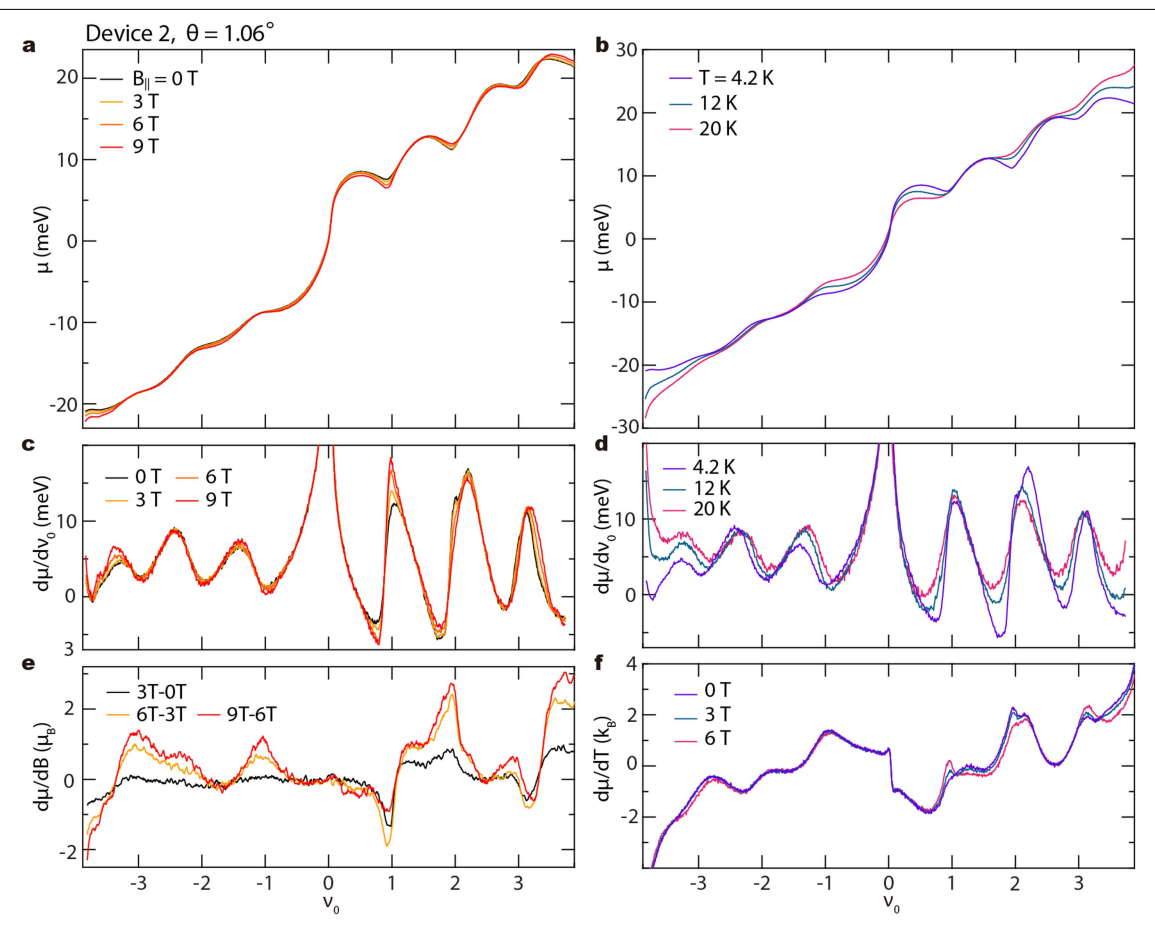
Extended Data Fig. 4 | **In-plane magnetic field dependence of the Hall density in device 1. a, b,** Hall density $\nu_{\rm H}$ (**a**) and subtracted Hall density $\nu_{\rm H} - \nu_0$ (**b**) expressed in electrons per superlattice unit cell, and measured with $B_{\rm tot} = 0.5$, 3, 6, 9 and 12 T and fixed $B_\perp = 0.5$ T. **c**, $\nu_{\rm H} - \nu_0$ as a function of $B_{\rm tot}$ and ν_0 with the magnetic field applied at an angle $\theta_B = 20.5^{\circ}$, measured at a nominal

T= 20 mK. Blue and pink circles correspond to the positions of peaks of ρ_{xx} and the points of maximum descent in $\nu_{\rm H}$ – $\nu_{\rm O}$, respectively, and denote phase boundaries between symmetry-breaking isospin ferromagnets (IF₁, IF₂ and IF₃) and an isospin unpolarized state (IU).



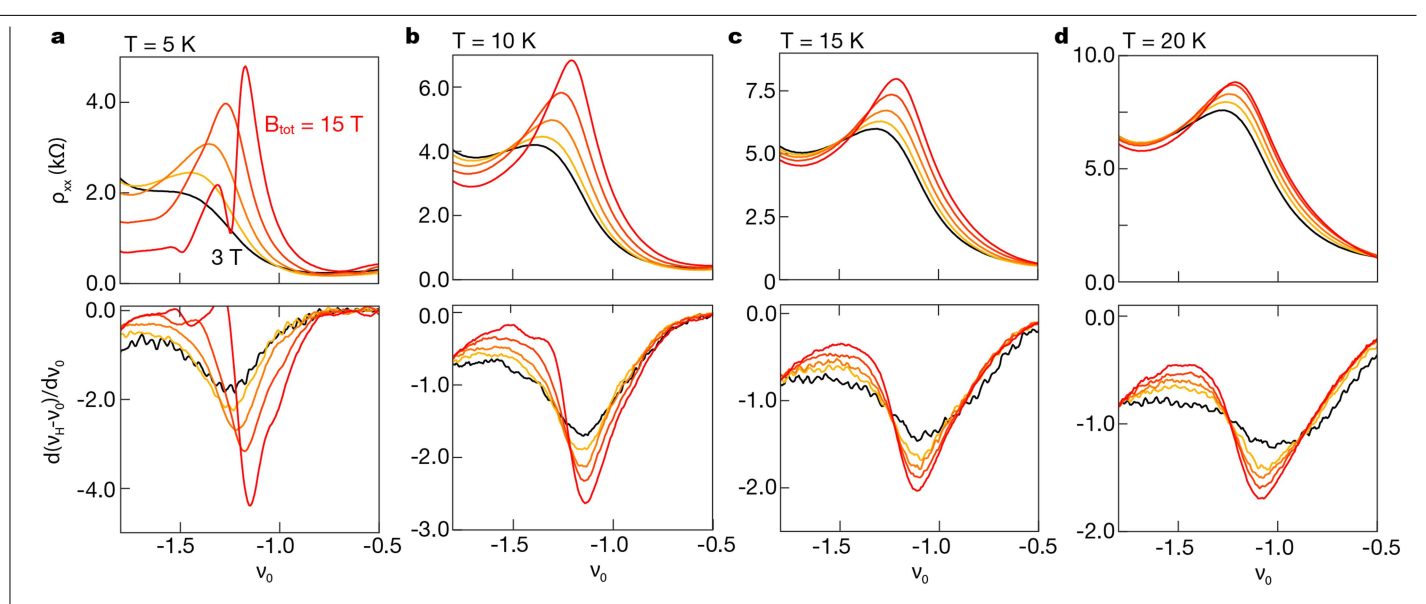
Extended Data Fig. 5 | **Landau fan diagram at the hole side in a tilted magnetic field in device 1.** a, ρ_{xx} as a function of ν_0 and total magnetic field B_{tot} oriented at an angle with respect to the plane θ_B of 4.1°(a), 9.6°(b) and 20.5°(c).

 $\label{eq:d-f} \textbf{d-f}, Schematics of the Landau fan diagram based on \textbf{a-c}, respectively.$ The numbered labels denote the Bloch band filling index, which encodes the number of electrons bound to each lattice unit cell.



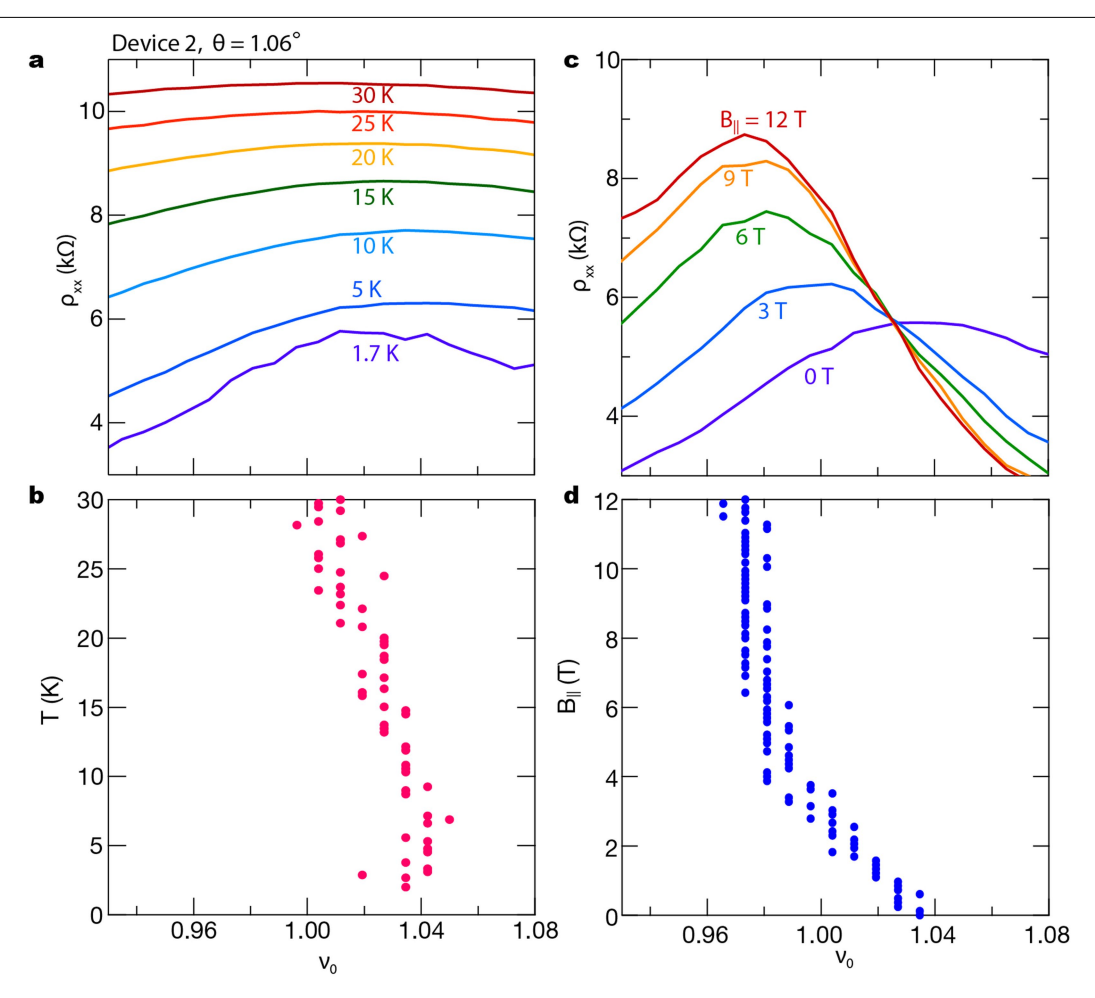
Extended Data Fig. 6 | **Thermodynamic measurements in device 2. a**, Chemical potential μ as a function of v_0 at T = 4.2 K and B_{\parallel} = 0, 3, 6 and 9 T. **b**, μ as a function of v_0 at B = 0 T and T = 4.2, 12 and 20 K. **c**, Inverse compressibility $d\mu/dv$ as a function of v_0 at T = 4.2 K and B_{\parallel} = 0, 3, 6 and 9 T.

d, $d\mu/dv$ as a function of v_0 at B=0 T and T=4.2, 12 and 20 K. **e**, $d\mu/dB_{\parallel}$ as a function of v_0 at T=4.2 K, calculated from $(\mu(9\text{ T})-\mu(6\text{ T}))/3$ T, $(\mu(6\text{ T})-\mu(3\text{ T}))/3$ T and $(\mu(3\text{ T})-\mu(0\text{ T}))/3$ T, **f**, $d\mu/dT$ as a function of v_0 , calculated from $(\mu(12\text{ K})-\mu(4.2\text{ K}))/7.8$ K at $B_{\parallel}=0$, 3 and 6 T.



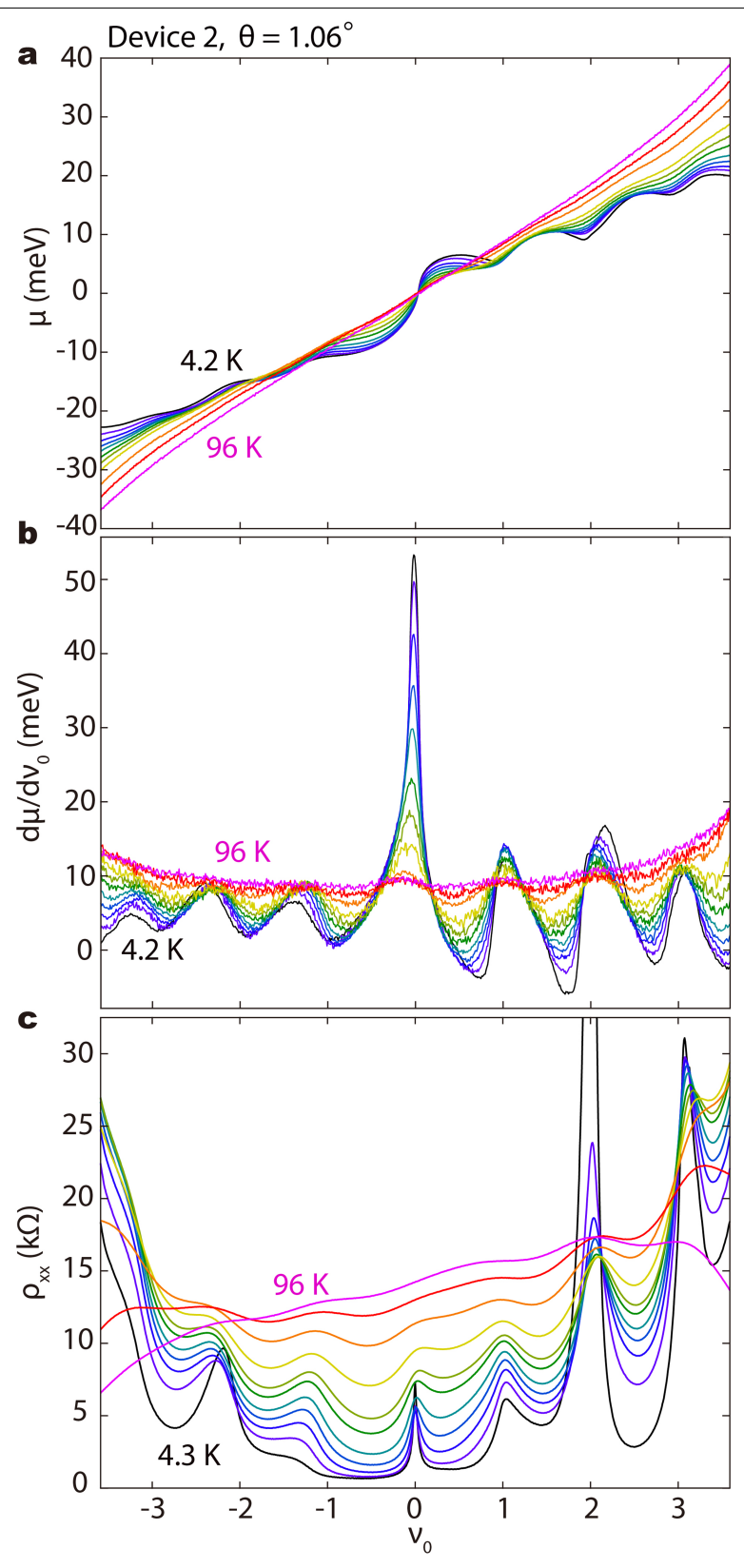
Extended Data Fig. 7 | **High-temperature transport in a tilted magnetic field in device 1.** a–d, ρ_{xx} (top) and $d(\nu_H - \nu_0)/d\nu_0$ (bottom) as a function of ν_0 at T=5 K (a), 10 K (b), 15 K (c) and 20 K (d) at $B_{tot}=3$, 6, 9, 12 and 15 T, oriented at an

angle of 9.1° relative to the plane. d($\nu_{\rm H}$ – ν_0)/d ν_0 is calculated from $\nu_{\rm H}$ – ν_0 using a 20-point moving average in ν_0 .



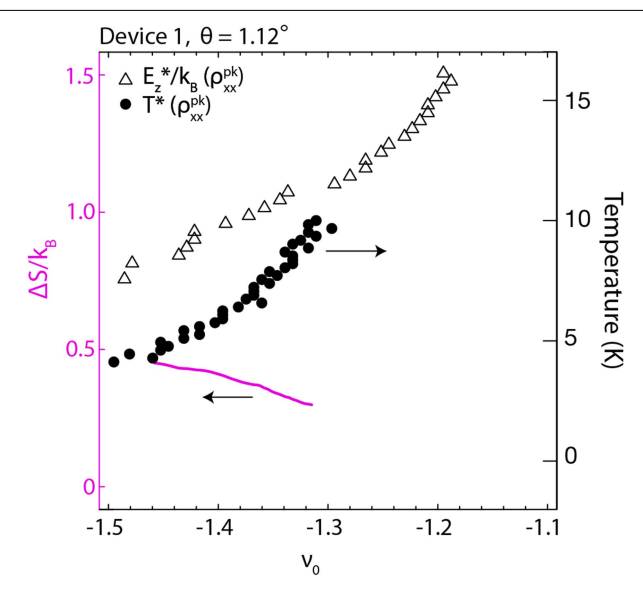
Extended Data Fig. 8 | Temperature and in-plane magnetic field dependence of resistive peak around v_0 = +1 in device 2. a, ρ_{xx} as a function of nominal filling factor v_0 around v_0 = +1 between 1.7 and 30 K in device 2. b, The

 ho_{xx} peak position as a function of v_0 and T. \mathbf{c} , ρ_{xx} as a function of nominal filling factor v_0 around v_0 = +1 at B_{\parallel} = 0, 3, 6, 9 and 12 T. \mathbf{d} , The ρ_{xx} peak position as a function of v_0 and B_{\parallel} .



Extended Data Fig. 9 | **Temperature-dependent chemical potential and resistance in device 2. a**, Chemical potential μ as a function of ν_0 at 4.2, 8.0, 12, 16, 20, 26, 32, 40, 59, 76 and 96 K. d μ /d ν_0 in Fig. 4 is calculated by the derivative

of these data. **b**, Inverse electronic compressibility d μ /d ν as a function of ν_0 at 4.2, 8,12,16, 20, 26, 32, 40, 59, 76 and 96 K. **c**, ρ_{xx} as a function of ν_0 at 4.3, 8.0, 12, 16, 20, 26, 31, 40, 59, 76 and 96 K.



Extended Data Fig. 10 | **Entropy change per superlattice unit cell** $\Delta S/k_{\rm B}$ **from the transport data.** White triangles and black circles are phase boundaries for the Zeeman-tuned transition $(E_Z^*/k_{\rm B})$ and temperature-tuned transition (T^*) , respectively, determined by the ρ_{xx} peak near ν = -1. The pink curve is $\Delta s/k_{\rm B}$ as a function of ν_0 , determined by equation (7).